Transport in Porous Media (2020) 134:173–194
https://doi.org/10.1007/s11242-020-01441-w

A Data-Driven Multiscale Framework to Estimate Effective Properties of Lithium-Ion Batteries from Microstructure Images

Svyatoslav Korneev[1,2] · Harikesh Arunachalam[1,3] · Simona Onori[1] · Ilenia Battiato[1]

Received: 7 November 2019 / Accepted: 24 June 2020 / Published online: 9 July 2020

Abstract
The Bruggeman model is routinely employed to determine transport parameters in macroscale electrochemical models. Yet, it relies on both a simplified representation of the porescale structure and specific hypotheses on the transport dynamics at the pore scale. Furthermore, its inherent scalar nature prevents it from capturing the impact that pore-structure anisotropy has on transport. As a result, the complex topology of electrochemical storage devices, combined with the broad range of conditions in which batteries operate, renders the Bruggeman relationship approximate, at best. We propose a self-consistent multiscale framework, based on homogenization theory, which a priori allows one to calculate effective parameters of battery electrodes for a range of transport regimes while accounting for full topological information at the pore scale. The method is based on the solution of a closure problem on a translationally periodic unit cell and generalized to handle locally non-periodic structures. We compare the Bruggeman and the closure-problem predictions of the effective diffusivity for a set of 18,000 synthetically generated images and propose a data-driven polynomial function correlating porosity and effective diffusivity, as calculated from a solution of the closure problem. We test its predictive capability against measured diffusivity values in a $LiCoO_2$ cathode and a Ni-YSZ anode.

Keywords Lithium-ion battery · Electrochemical modeling · Homogenization · Closure variable resolution · Scanning electron microscopy · Bruggeman effective medium theory

1 Introduction

Lithium-ion rechargeable batteries are the most promising energy storage technology today and their application spans from consumer electronics to electrified propulsion systems (Sbarufatti et al. 2017). Yet, growth of the global electric vehicle market has been slower

✉ Ilenia Battiato
ibattiat@stanford.edu

[1] Energy Resources Engineering, Stanford University, Stanford, CA 94305, USA

[2] Present Address: PARC, Palo Alto, CA 94304, USA

[3] Present Address: Rivian Automotive LLC, Irvine, CA 92618, USA

than initially predicted in the beginning of this decade (Choi and Aurbach 2016). From a materials perspective, lithium-ion technology has matured significantly and has begun to reach its theoretical energy limits (Fotouhi et al. 2016). Ongoing electrochemical research in the transportation industry is focused on enhancing battery life cycle, safety, and other performance characteristics to enhance its market penetration. This is possible through the development of an effective battery management system (BMS), for which advanced electrochemical battery modeling and estimation techniques are vital to push batteries to operate at their physically permissible limits (Zheng et al. 2016). Prediction of the capabilities of batteries during design or utilization is dependent on the accurate modeling of Li-ion transport at relevant scales. In this context, the pinnacle of model prediction capability is determined by the accuracy of (1) the models employed and (2) the estimation or measurement of model parameters.

The battery research community, for long, has considered the Doyle–Fuller–Newman (DFN) macroscale model (Doyle et al. 1993; Doyle and Newman 1995), and its subsequent generalizations, as the benchmark. Since the inception of the DFN model, the effective transport coefficients Ψ_{eff} of battery electrodes needed for its parameterization have been determined from their intrinsic (pore scale) counterparts Ψ (Vijayaraghavan et al. 2012) as

$$\Psi_{\text{eff}} = \frac{\phi}{\tau}\Psi, \tag{1}$$

where ϕ is the porosity and τ is the tortuosity. The latter is defined as the ratio between an effective path length ℓ_{eff} to the Euclidean length (straight-line length) of a control volume. Although routinely employed, (1) it requires the knowledge of the pore scale structure, historically unavailable until the advent of X-ray tomography (XCT) and scanning electron microscopy (SEM), and (2) it is ambiguous since ℓ_{eff} depends on the transport process occurring in the microstructure and may not be able to be consistently defined when multiple transport processes are occurring at the same time (Sharratt and Mann 1987; Valdés-Parada et al. 2011). The general difficulty in estimating tortuosity led to the widespread use of the classical Bruggeman relationship

$$\tau = \phi^{-\alpha}, \tag{2}$$

between tortuosity τ and porosity ϕ, the latter being a quantity much easier to measure. In (2), α is the Bruggeman exponent, equal to 0.5 for perfectly spherical particles. While the use of the relationship has allowed one to seemingly circumvent the often problematic definition of tortuosity, it has introduced a number of additional complications. For example, the Bruggeman equation, in its original formulation, neglects the influence of the particle morphology and orientation and it cannot capture the impact of anisotropic effective parameters, due to its intrinsic scalar formulation.

The main advantage of (2) that has led to its popularity lies in its simplicity, ease of use, and its underlying conceptualization that averaged topological descriptors of the microstructure (i.e., porosity and tortuosity) can be related to properties controlling the dynamical response of the system at a larger scale. Yet, experimental investigations have revealed that the topology and geometry of electrode constituents play a significant role in battery dynamical response (Shearing et al. 2010; Wilson et al. 2011): On the one hand, electrodes with the same volume fraction can have significantly disparate performance due to differences in pore-space topology, and on the other, electrode particles topology and geometrical configuration vary over battery life due to volume changes, cracks, and stress–strain effects that result from cyclic charge and discharge. As a result, the validity

of the Bruggeman relationship has lately come under close scrutiny in the battery community where both numerical (Chung et al. 2013; Cooper et al. 2014) and laboratory experiments (Abraham 1993; Stephenson et al. 2007; Djian et al. 2007) showed significant discrepancies between the measured and predicted tortuosity through the classical Bruggeman model. For example, DuBeshter et al. (2014) conducted experiments to characterize the electrode MacMullin number for commercial battery electrodes. The results show substantially higher tortuosity values than the classical Bruggeman approach (Kehrwald et al. 2011), emphasizing the need for estimating electrode properties through experiments rather than empirical formulations. Malifarge et al. (2017) synthesized symmetric coin cells and conducted impedance measurements between a frequency range of 1 MHz and 1 mHz using a 5 mV perturbation amplitude. A transmission line model was used to fit the measured impedance spectra using nonlinear fitting to minimize the error between the experimental and model-predicted response. The tortuosities obtained using this approach were significantly higher than those reported using the classical Bruggeman relationship. Landesfeind et al. (2016) conducted impedance measurements to estimate the tortuosity of commercial separator materials. Results indicate that the classical Bruggeman relationship significantly under-predicts the tortuosity values across the porous separators. While direct experimental measurements of effective parameters (and/or tortuosity) are invaluable, associated high cost limits their practical deployment as methods to routinely estimate effective model parameters.

The advent of techniques such as XCT (and SEM) has enabled one to directly estimate model parameters (e.g., tortuosity, effective diffusivity) on realistic high-resolution images of electrode microstructures (Terborg et al. 2013; Stiaszny et al. 2014a, b; Grützke et al. 2015), while validating various modeling approximations through computer simulations at a fraction of the cost (see review on computational methods by Grazioli et al. (2016), and references therein). A number of studies on non-spherical active particle electrodes have reported significant deviation between measured tortuosity and that estimated from the Bruggeman approach (García-García and García 2016; Stephenson et al. 2007; DuBeshter et al. 2014). Extensive research, both analytical and numerical, has ensued on the wake of improving estimates of tortuosity and effective coefficients associated with lithium transport between electrodes. Vijayaraghavan et al. (2012) derived analytical expressions for tortuosity in low and high porosity electrodes by incorporating filler materials (carbon black) in the porous matrix. Ebner and Wood (2015) developed a software tool, *BruggemanEstimator*, to estimate in-plane and out-of-plane Bruggeman exponents based on the differential effective medium approximation using microscopic images of the top and the cross section of battery electrodes. Bucci et al. (2017) used random walk analysis to estimate the impact of microcracks on the effective conductivity of composite electrodes. Chung et al. (2013) used a finite element model to analyze the tortuosities of 3-D reconstructions of experimentally fabricated porous electrodes. These investigations revealed that inhomogeneities in particle packing and polydispersity result in an increase in the overall tortuosity. Cooper et al. (2013) compared five approaches to quantify the tortuosity factor: While three of the methods showed strong correlations, they provided consistently different values. Thorat et al. (2009) proposed a generalized Bruggeman relation, $\tau = A\phi^{-B}$ to improve predictions of the measured tortuosities. A similar approach was later proposed by Vijayaraghavan et al. (2012) with a Bruggeman relationship in the form $\tau = \gamma\phi^{1-\alpha}$, where the coefficients γ and α are determined by fitting the tortuosity values obtained through numerical simulations across a range of electrode porosities.

Despite a general awareness that tortuosity–porosity relationships are, at best, simplistic representations of a more complex topology, a recent review by Tjaden et al. (2016) on the

derivation of Bruggeman relationship in its most popular form warns on its limitations, which "are not widely appreciated" (Tjaden et al. 2016). For example, the relatively small sensitivity of the tortuosity factor to large variations of porosity (0.3-0.7) may lead to misinterpreting any accidental agreement between predicted and measured tortuosity for an experimental validation of the Bruggeman correlation (Tjaden et al. 2016). In addition, the authors highlight that the approximations in the Bruggeman relationship do not entail exclusively topological simplifications (e.g., assuming that the obstructions are spherical or cylindrical), but also assumptions on the transport dynamics. The latter problem has seeped through almost undetected, since the majority of the works in the electrochemical community have primarily focused on the impact of the spherical particle hypothesis. As emphasized by Tjaden et al. (2016), the Bruggeman model is derived for diffusion-dominated transport. This critical observation directly connects with the large body of work acknowledging the challenge of properly defining tortuosity in different transport regimes.

The lack of uniqueness in the definition of tortuosity, including its dependence on pore-scale transport processes, has been long known in the fields of civil engineering and geosciences (Darcy 1856; Bear 1972): The review of several definitions of tortuosity can be found in Dullien (1992), Clennel (1997), which include the concepts of geometrical (Adler 1992), hydraulic (Kozeny 1927; Carman 1937), diffusive (Penman 1940; Petersen 1958), dispersive (Bear 1969; Greenkorn 1983), and electrical tortuosities (Archie 1942).

A review on the different definitions of tortuosity is provided by Ghanbarian et al. (2012). Valdés-Parada et al. (2011) showed the impact that different transport regimes (diffusive, advective, and reactive) have on tortuosity calculations and discussed the appropriateness of introducing the concept of tortuosity in different transport scenarios. Importantly, they discuss the challenges of consistently defining the concept of tortuosity when more than one transport process is taking place. For example, Sharratt et al. (1987, Fig. 18), who studied reactive mass transport in catalytic particles, found that tortuosity is function of the reaction rate and may have values smaller than one. Similar conclusions were reached by Edwards et al. (1993) in the context of dispersion and reaction in porous media.

While a number of works have focused on relaxing the spherical/cylindrical grain hypothesis by constructing generalizations of the Bruggeman relationship for non-spherical and polydisperse media (Chung et al. 2013; Stephenson et al. 2007; Ebner et al. 2014), the purely diffusive-transport hypothesis probably remains the most stringent assumption when applying such a model to batteries, which are, more often than not, characterized by diffusion-limited regions due to both active material and pore-space polydispersity or both (Garcia et al. 2005; Chung et al. 2014; Yu et al. 2016), and operating conditions (e.g., high C-rates) (Garcia and Chiang 2007; Jiang and Peng 2016), or dispersive effects as in flow batteries.

Upscaling methods (Battiato et al. 2009; Battiato and Tartakovsky 2011; Boso and Battiato 2013; Arunachalam et al. 2015; Korneev and Battiato 2016) provide both a mathematical framework to connect pore-scale processes to effective medium (upscaled) equations as well as rigorous definitions, under different dynamic conditions, of their effective transport parameters whose dependence on local pore-scale topology can be explicitly accounted for. This is achieved, as described in Korneev and Battiato (2016), Arunachalam et al. (2017), Zhang and Tartakovsky (2017a), by directly solving a boundary value problem, or closure problem, on a representative microstructure without the need of introducing topological intermediaries, such as tortuosity. Zhang et al. (2017); Zhang and Tartakovsky (2017b) employed homogenization theory in the context of microscale materials design to maximize energy/power

density performance in electrochemical devices. Arunachalam et al. (2017) showed that even a minor degree of polydispersity in an idealized microstructure of spherical particles can lead to approximately 20% difference between the effective transport parameters determined by Bruggeman relationship and through rigorous upscaling. In Arunachalam and Onori (2019), it was shown that the solution of the pore-scale closure problem to calculate the effective diffusion and conductivity parameters of NMC cathode batteries leads to more accurate prediction capability when compared to DFN model under diverse battery operating conditions.

In this work, we aim at determining effective coefficients from microstructural images of lithium-ion battery electrodes in the context of homogenization theory. Unlike other works, the approach proposed allows one to either directly bypass the, often ambiguous, concept of tortuosity, or rigorously generalize it in the context of homogenization theory, i.e., in a way mathematically consistent with the macroscopic equations to be parameterized. We do so by expressing tortuosity (or any macroscale effective parameter) in terms of a closure variable, a tensorial quantity derived by solving a boundary value problem (BVP) on a representative volume of the electrode. The approach has two primary advantages: (1) The tensorial nature of the closure variable allows one to account for anisotropy on cells of arbitrary structures without any postulation about the nature of anisotropy and (2) the direct solution of the BVP on a representative volume of the electrode allows one to account for the topological and morphological complexity of particles shape. Importantly, the so-defined tortuosity is self-consistent with the upscaled equation it parameterizes through a regime-specific BVP, i.e., different upscaled equations (which may account for different dynamics) will lead to BVP of different form and different values of tortuosity for the same structure. We then apply the method to a set of synthetically generated statistically isotropic pore-scale structures to improve upon Bruggeman relation, while retaining the benefits of its simple structure.

The paper is structured as follows. Section 2 summarizes the mass and charge transport equations at the pore- and continuum scale in the electrolyte in the context of homogenization theory. We also introduce the definition of effective parameters as the spatial averages of a closure variable, which is the solution of a properly defined boundary value problem in a representative domain at the pore scale. In Sect. 3, the validity of the classical Bruggeman relationship is assessed against the closure variable approach, and a data-driven modified polynomial expression is proposed to improve the fitting of the dispersion–porosity relationship, when computational cost is a major concern. Section 4 presents the evaluation of the dispersion tensor components for realistic microstructures obtained through SEM images available in the literature. Section 5 summarizes the conclusions of this work.

2 Lithium-Ion Transport Model from Pore to Continuum Scale

In this section, we report, for completeness, the set of equations governing charge and Li-ion mass transport in the electrolyte at both the pore scale and continuum scale. We emphasize that the continuum-scale equations are those derived within the homogenization framework by multiple-scale expansion of Arunachalam et al. (2015). A similar set of equations for the electrode can be found in Arunachalam et al. (2015).

2.1 Pore- and Continuum-Scale Equations

The pore-scale mass and charge transport of lithium ions in the electrodes and the electrolyte are governed by the Poisson–Nernst–Planck (PNP) equations of material balance and electroneutrality (Less et al. 2012). Based on the homogenization approach, the porous electrode is assumed to be composed of spatially periodic unit cells of characteristic dimension ℓ. Each unit cell may consist of multiple active electrode particles of arbitrary shape and configuration that are surrounded by the electrolyte phase $\mathcal{B}$ and separated by an interface Γ. We define the scale separation parameter

$$\varepsilon = \frac{\ell}{L} \ll 1, \tag{3}$$

where L is the characteristic size of the macroscopic domain, e.g., the entire electrode, and ε can be interpreted as the dimensionless size of a repeating unit cell, see Fig. 1. The union of all unit cells forms a connected pore-space $\mathcal{B}^\varepsilon$. The union of all the solid–liquid interfaces in $\mathcal{B}^\varepsilon$ is defined as Γ^ϵ.

The dimensionless concentration of lithium and electric potential in the electrolyte, c_ε^e and ϕ_ε^e, at location $\mathbf{x} \in \mathcal{B}^\epsilon$ and time t, defined as $c_\varepsilon^e := \hat{c}_\varepsilon^e / \hat{c}_{\max}^s$ and $\phi_\varepsilon^e := \hat{\phi}_\varepsilon^e F/(2RT)$ with $\hat{c}_\varepsilon^e$ and $\hat{\phi}_\varepsilon^e$ being the dimensional concentration and electric potential, satisfy the mass and charge transport equations (Arunachalam et al. 2015)

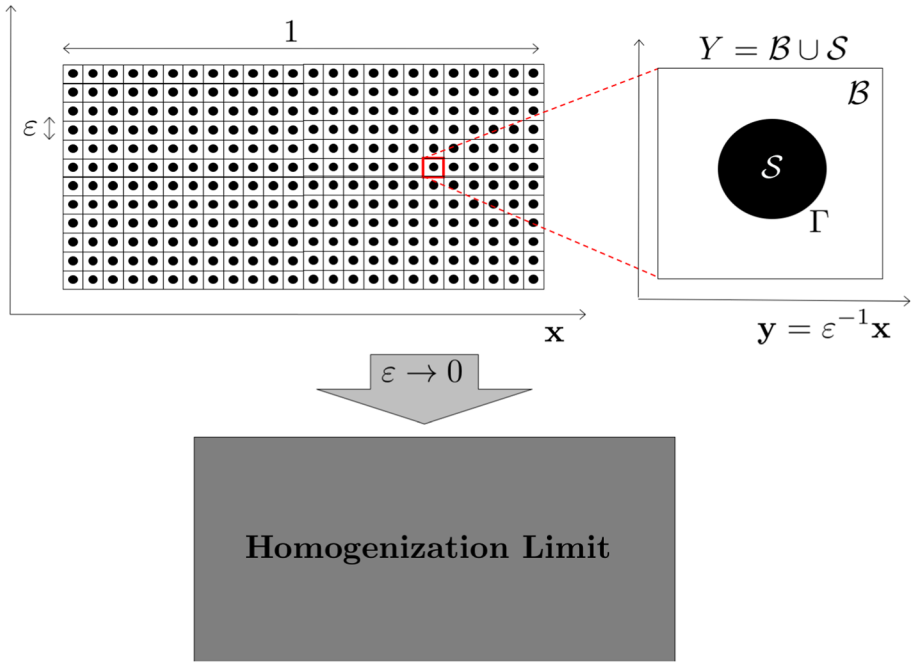

Fig. 1 Conceptualization of the homogenization process on a periodic structure (adapted from Battiato et al. 2019). Although depicted as an array of repeating unit cells containing one spherical particle, the unit cell structure can be arbitrarily complex

$$\frac{\partial c_\varepsilon^e}{\partial t} = \nabla \cdot [(\mathbf{D}^e + \lambda t_+^2 \mathrm{Pe}_e \mathbf{K}^e / c_\varepsilon^e) \nabla c_\varepsilon^e + 2\mathrm{Pe}_e t_+ \mathbf{K}^e \nabla \phi_\varepsilon^e], \quad \mathbf{x} \in \mathcal{B}^\epsilon \tag{4a}$$

$$0 = \nabla \cdot [(\lambda t_+ \mathbf{K}^e / c_\varepsilon^e) \nabla c_\varepsilon^e + 2\mathbf{K}^e \nabla \phi_\varepsilon^e], \quad \mathbf{x} \in \mathcal{B}^\epsilon \tag{4b}$$

subject to

$$\mathbf{n}_e \cdot [(\mathbf{D}^e + \lambda t_+^2 \mathrm{Pe}_e \mathbf{K}^e / c_\varepsilon^e) \nabla c_\varepsilon^e + 2\mathrm{Pe}_e\, t_+ \mathbf{K}^e \nabla \phi_\varepsilon^e] = \mathrm{Da}_e f(c_\varepsilon^e, c_\varepsilon^s, \phi_\varepsilon^s, \phi_\varepsilon^e), \tag{5a}$$

$$\mathbf{n}_e \cdot [(\mathrm{Pe}_e \lambda t_+ \mathbf{K}^e / c_\varepsilon^e) \nabla c_\varepsilon^e + 2\mathrm{Pe}_e \mathbf{K}^e \nabla \phi_\varepsilon^e] = \mathrm{Da}_e f(c_\varepsilon^e, c_\varepsilon^s, \phi_\varepsilon^s, \phi_\varepsilon^e), \tag{5b}$$

on Γ^ϵ, respectively. In (4) and (5), all temporal and spatial scales are rescaled by the macroscopic length L and the diffusion time in the electrolyte phase $\hat{t}_{D_e}$, respectively, i.e., $\mathbf{x} = \hat{\mathbf{x}}/L$ and $t_e = \hat{t}/\hat{t}_{D_e}$; also, $\mathbf{D}^e = \hat{\mathbf{D}}^e/D^e$ and $\mathbf{K}^e = \hat{\mathbf{K}}^e/K^e$ are the dimensionless interdiffusion coefficient and the electric conductivity in the electrolyte, while the hatted quantities are their dimensional counterparts with $D^e = \mathcal{O}(\hat{\mathbf{D}}^e)$ and $K^e = \mathcal{O}(\hat{\mathbf{K}}^e)$. Also, $\hat{c}^s_{\max}$ is the maximum concentration of lithium that can be stored in the active particle. The Butler–Volmer equation, which controls ion transport across the electrode–electrolyte boundaries, is

$$f(c_\varepsilon^e, c_\varepsilon^s, \phi_\varepsilon^e, \phi_\varepsilon^s) = 2\sqrt{c_\varepsilon^e c_\varepsilon^s (1 - c_\varepsilon^s)}\, \sinh(\phi_\varepsilon^s - \phi_\varepsilon^e - U), \tag{6}$$

where $U = F\hat{U}/(2RT)$ is the dimensionless open-circuit potential, $c_\varepsilon^s := \hat{c}_\varepsilon^s/\hat{c}^s_{\max}$ and $\hat{c}_\varepsilon^s$ are the dimensionless and dimensional electrode particle concentration, respectively, and the dimensionless Damköhler and electric Péclet numbers are defined as follows

$$\mathrm{Da}_e := \frac{Lk}{FD^e} \quad \text{and} \quad \mathrm{Pe}_e := \frac{RTK^j}{F^2 D^j \hat{c}^s_{\max}}, \tag{7}$$

where k ($\mathrm{Vm\Omega^{-1}mol^{-1}}$) is the electrochemical reaction rate constant that describes the kinetics of lithium-ion transfer on Γ^ϵ; $\hat{U}$ (V) is the open-circuit potential; t_+ is the transference number, $\lambda := 1 + \dfrac{\mathrm{d}\ln f_\pm}{\mathrm{d}\ln(\hat{c}_\varepsilon^e/\hat{c}^s_{\max})}$ is treated as constant; and $f_\pm$ is the activity coefficient; $\mathbf{n}_e$ is the outward unit normal vector to Γ^ϵ pointing from the electrolyte towards the active particle; F and R are the Faraday and the universal gas constants; and T is the temperature. A detailed derivation of Equations (4), (5) and (6) from the dimensional Poisson–Nernst–Planck equations with Butler–Volmer dynamics can be found in Arunachalam et al. (2015, Eqs. (1) to (10)).

The method of homogenization by multiple-scale expansions is based on the ansatz that each (dimensionless) pore-scale quantity ψ_ε can be expanded in an infinite series in integer powers of ε, i.e., for any microscale variable, a multiple-scale asymptotic expansion is an ansatz of the form,

$$\psi_\varepsilon(\hat{\mathbf{x}}, t) := \psi(\mathbf{x}, \mathbf{y}, t) = \sum_{m=0}^{\infty} \varepsilon^m \psi_m(\mathbf{x}, \mathbf{y}, t) = \psi_0(\mathbf{x}, \mathbf{y}, t) + \varepsilon\psi_1(\mathbf{x}, \mathbf{y}, t) + \varepsilon^2\psi_2(\mathbf{x}, \mathbf{y}, t) + \cdots \tag{8}$$

wherein each function $\psi_m(\mathbf{x}, \mathbf{y}, t)$ in this series depends on two variables, $\mathbf{x}$, the macroscopic (or slow) variable and $\mathbf{y}$, the microscopic (or fast) variable defined as

$$\mathbf{y} = \varepsilon^{-1}\mathbf{x}, \tag{9}$$

and $\psi_m(\mathbf{x}, \mathbf{y}, t)$, $m = 0, 1, \ldots$, are Y-periodic in $\mathbf{y}$. Then, the homogenized (or upscaled or macroscopic) equation for a pore-scale quantity ψ_ε is obtained by determining the following limit,

$$\langle \psi \rangle = \langle \lim_{\varepsilon \to 0} \psi_\varepsilon \rangle, \tag{10}$$

where $\langle \cdot \rangle$ is an average defined over the unit cell, see Fig. 1.

Under appropriate hypotheses (Arunachalam et al. 2015), lithium transport in the electrolyte phase described by (4) and (5) can be homogenized, i.e., approximated up to errors of order ε^2, by the following effective mass and charge transport equations

$$\begin{aligned} \eta \partial_t \langle c^e \rangle_{\mathcal{B}} = \nabla_{\mathbf{x}} \cdot [(\mathbf{D}^\star + \varepsilon^{-\alpha} \lambda t_+^2 \mathbf{K}^\star / \langle c^e \rangle) \nabla_{\mathbf{x}} \langle c^e \rangle_{\mathcal{B}} + 2\varepsilon^{-\alpha} t_+ \mathbf{K}^\star \nabla_{\mathbf{x}} \langle \phi^e \rangle_{\mathcal{B}}] \\ + 2\eta \varepsilon^{-1} \mathcal{K}^\star \mathrm{Da}_e f(\langle c^e \rangle_{\mathcal{B}}, \langle c^s \rangle_s, \langle \phi^e \rangle_{\mathcal{B}}, \langle \phi^s \rangle_s), \end{aligned} \tag{11}$$

and

$$\begin{aligned} \mathrm{Pe}_e \nabla_{\mathbf{x}} \cdot [(\lambda t_+ \mathbf{K}^\star / \langle c^e \rangle) \nabla_{\mathbf{x}} \langle c^e \rangle_{\mathcal{B}} + 2\mathbf{K}^\star \nabla_{\mathbf{x}} \langle \phi^e \rangle_{\mathcal{B}}] \\ = 2\eta \varepsilon^{-1} \mathcal{K}^\star \mathrm{Da}_e f(\langle c^e \rangle_{\mathcal{B}}, \langle c^s \rangle_s, \langle \phi^e \rangle_{\mathcal{B}}, \langle \phi^s \rangle_s), \end{aligned} \tag{12}$$

with

$$f(\langle c^e \rangle_{\mathcal{B}}, \langle c^s \rangle_s, \langle \phi^e \rangle_{\mathcal{B}}, \langle \phi^s \rangle_s) = 2\sqrt{\langle c^e \rangle_{\mathcal{B}} \langle c^s \rangle_s (1 - \langle c^s \rangle_s)} \sinh(\langle \phi^s \rangle_s - \langle \phi^e \rangle_{\mathcal{B}} - U), \tag{13}$$

and

$$\begin{aligned} \langle \mathcal{A} \rangle_e &\equiv \frac{1}{|Y|} \int_{\mathcal{B}(\mathbf{x})} \mathcal{A} \mathrm{d}\mathbf{y}, \quad \langle \mathcal{A} \rangle_s \equiv \frac{1}{|Y|} \int_{\mathcal{S}(\mathbf{x})} \mathcal{A} \mathrm{d}\mathbf{y}, \\ \langle \mathcal{A} \rangle_{\mathcal{B}} &\equiv \frac{1}{|\mathcal{B}|} \int_{\mathcal{B}(\mathbf{x})} \mathcal{A} \mathrm{d}\mathbf{y}, \quad \langle \mathcal{A} \rangle_{\mathcal{S}} \equiv \frac{1}{|\mathcal{S}|} \int_{\mathcal{S}(\mathbf{x})} \mathcal{A} \mathrm{d}\mathbf{y}, \end{aligned} \tag{14}$$

where $\mathcal{A}(\mathbf{x})$ is a pore-scale quantity, provided the following conditions are met:

1. $\varepsilon \ll 1$,
2. $\mathrm{Da}_e < 1$,
3. $\mathrm{Pe}_e < 1$,
4. $\mathrm{Da}_e / \mathrm{Pe}_e < 1$,

Constraints (1)–(4) ensure the separation of scales. While constraint (1) is almost always met in practical applications since the pore size is generally much smaller that the electrode dimension, constraints (2)–(4) depend on the relative importance of the diffusion, electromigration, and reaction mechanisms, i.e., they impose constraints on the transport regimes that can be appropriately modeled by the continuum scale equations (11) and (12) within errors of order ε^2. Details of the derivation can be found in "Appendix" of Arunachalam et al. (2015).

2.2 Effective Coefficients

The effective coefficients in (11) can be rigorously defined within the context of homogenization theory as follows. The dimensionless effective reaction rate constant in the electrolyte phase $\mathcal{K}^\star$ is determined by the pore geometry as $\mathcal{K}^\star = |\Gamma|/|\mathcal{B}|$. The effective diffusion and electromigration tensors are given by

$$\begin{aligned} \mathbf{D}^\star &= \langle \mathbf{D}^e(\mathbf{I} + \nabla_{\mathbf{y}}\boldsymbol{\chi})\rangle_e, \\ \mathbf{K}^\star &= \langle \mathbf{K}^e(\mathbf{I} + \nabla_{\mathbf{y}}\boldsymbol{\chi})\rangle_e, \end{aligned} \tag{15}$$

where the closure variable $\boldsymbol{\chi}(\mathbf{y})$ has zero mean, $\langle \boldsymbol{\chi}\rangle_e = \mathbf{0}$, and is defined as a solution to the local problem in the unit cell Y

$$\nabla_{\mathbf{y}} \cdot (\nabla_{\mathbf{y}}\boldsymbol{\chi} + \mathbf{I}) = 0, \qquad \mathbf{y} \in \mathcal{B}, \tag{16a}$$

$$\mathbf{n}_e \cdot (\nabla_{\mathbf{y}}\boldsymbol{\chi} + \mathbf{I}) = 0, \qquad \mathbf{y} \in \Gamma, \tag{16b}$$

with $\mathbf{I}$ the identity matrix (Arunachalam et al. 2015), i.e., once the geometry of the unit cell Y is known, first the BVP (16) is solved to determine the closure variable $\boldsymbol{\chi}$, and then, the effective diffusion and conductivity coefficients are determined by calculating the spatial average of $\boldsymbol{\chi}$ over Y through (15). A schematic of the process is provided in Fig. 2. We emphasize that although Eq. (16) is a Poisson equation, general closure problems can be arbitrarily complex and include not only diffusion, but also other processes such as advection (see, e.g., Battiato and Tartakovsky 2011).

The advantage of the closure variable approach over empirical approaches, such as the Bruggeman approximation, lies in its ability to rigorously link effective coefficients

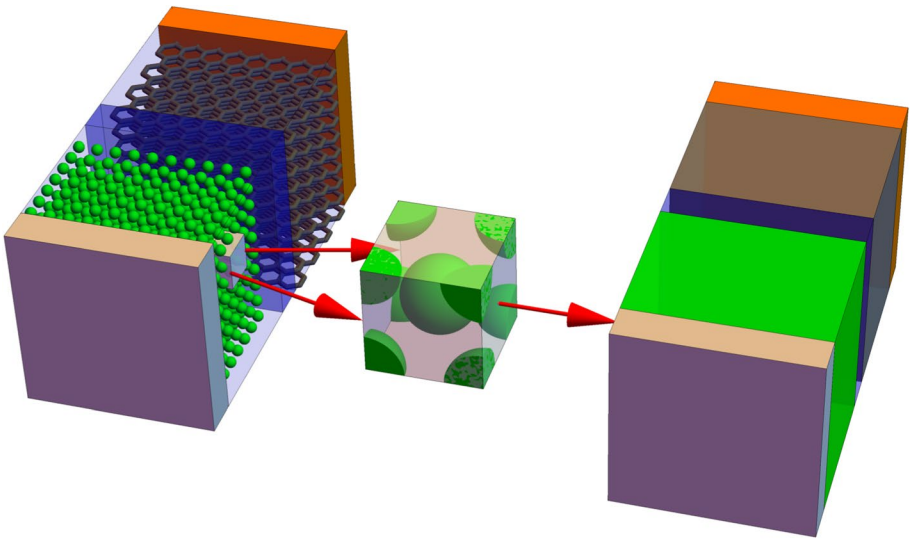

Fig. 2 Schematic representation of the homogenization procedure. First (from the left-hand side), a periodic "unit" cell is determined; second, the closure problem is solved in the "unit" to find the effective properties, of the continuous model

to different topological structures at the pore scale. The closure variable accounts for the impact of the microstructure and can be determined using *offline* calculations. As a result, the closure problem can be resolved as a preprocessing step and the effective parameter values can be directly incorporated in the homogenized model equations.

In the following, we provide a definition of tortuosity in the context of homogenization theory and propose a generalization of a Bruggeman-type relationship, which allows one to account for arbitrarily complex morphology of the electrode phase in the unit cell.

2.3 Closure Variable and Tortuosity

As previously emphasized, the primary advantage of the Bruggeman relation lies in its simplicity and ease of use. It is therefore convenient to recast (15) in the form of a Bruggeman-type relationship, without the imposition of additional restrictions on the pore-scale topology. Equation (15) can be written as

$$\mathbf{\Psi}_{\text{eff}} = \langle \mathbf{I} + \nabla_{\mathbf{y}} \boldsymbol{\chi} \rangle_e, \tag{17}$$

with $\mathbf{\Psi}_{\text{eff}}$ equal to $\mathbf{D}^\star$ or $\mathbf{K}^\star$, i.e., macroscopic coefficients depend on pore-scale geometry (not only on porosity) and they are tensors. Equation (1) should be interpreted as a definition of tortuosity, the latter being a quantity defined as inversely proportional to the dimensionless effective coefficient, namely

$$\tau := \frac{\phi}{\mathbf{\Psi}_{\text{eff}}}. \tag{18}$$

In analogy with (18), while using (17) and indicial notation, one can then provide a more general definition of tortuosity in the context of homogenization theory, i.e.,

$$\tau_{ii} = \frac{\phi}{\mathbf{\Psi}_{\text{eff},ii}} = \frac{\phi}{\left\langle I_{ii} + \dfrac{\partial \chi_i}{\partial y_i} \right\rangle_e} \tag{19}$$

where τ_{ii} are the diagonal components of the tortuosity tensor $\boldsymbol{\tau}$. It is worth emphasizing that off-diagonal components are zero since transport is only by diffusion. Using the definition for the averaging operator $\langle \cdot \rangle_e$ (14), Eq. (19) can be written as,

$$\tau_{ii} = \phi |Y| \left[\int_{\mathcal{B}} \left(I_{ii} + \frac{\partial \chi_i}{\partial y_i} \right) \mathrm{d}\mathbf{y} \right]^{-1}, \tag{20}$$

consistent with definitions obtained from other upscaling methods (Sun et al. 2013; Allen and Sun 2017). Similar results can be obtained with the method of volume averaging (Valdés-Parada et al. 2011) or any other upscaling method. It is worth emphasizing that although the concept of tortuosity could be entirely by-passed as the closure variable χ, and not tortuosity, is the critical variable necessary to define effective parameters, two comments ensue: (1) The right-hand side of Eq. (17) may be different depending on the problem under consideration (e.g., it could include advective terms as well), i.e., the method allows one to clearly define the tortuosity (be it diffusive, hydraulic, electric, etc.) consistent with the problem being upscaled, and (2) a relationship between tortuosity and closure variable can be always rigorously defined, as shown above.

In the following section, we use a set of synthetically generated images of two types of porous media (granular and fractured) to calculate their effective transport properties by using both the classical Bruggeman and the homogenization-based approach and show that the Bruggeman relationship cannot capture the correct functional dependence between porosity and effective properties, even for statistically isotropic media.

3 Validity of the Classical Bruggeman Relationship

To assess the ability of the classical Bruggeman relationship to determine the components of the dispersion tensor using porosity only, 18,000 synthetic images of random porous media are generated and the dispersion coefficient is determined using both Bruggeman and solving numerically the closure problem in Eq. (16). The synthetic medium is represented by a binary image of 360×360 pixel size, where the black regions correspond to the active material phase and the white regions correspond to the surrounding electrolyte phase. The set consists of two types of topologies of porous media. The first type is a granular porous medium (see Fig. 3), and the second is a low-porosity cracked porous medium (see Fig. 4). The porosity distribution of the set is close to a uniform distribution, where porosity is defined as the ratio between the area occupied by the electrolyte phase and the total area.

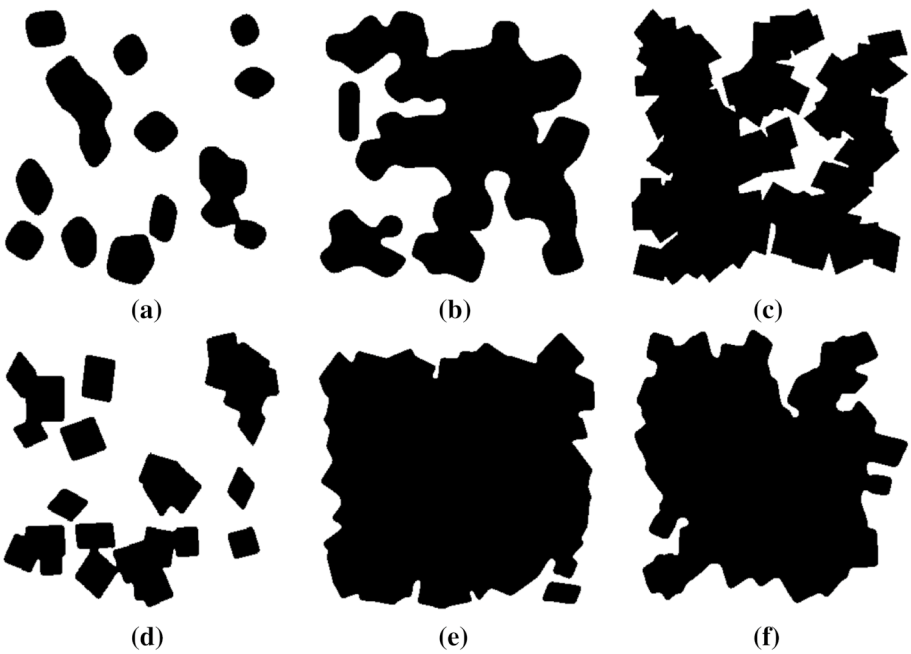

Fig. 3 Examples of the synthetic granular porous medium

Fig. 4 Examples of the synthetic low-porosity cracked porous medium

3.1 Image Generation Algorithm

Steps of the algorithm used to generate such images are represented in Fig. 5, and the code details are provided in "Appendix." In the first step, a binary image is generated by randomly placing filled parallelograms, see Fig. 5a. The number of parallelograms, their position, orientation, and aspect ratio are all random numbers extracted from a uniform distribution. In the next step, a Gaussian filter with a kernel of random width is applied to the binary image, see Fig. 5b. The third step involves the application of Otsu's segmentation of the grayscale image (Otsu 1979), Fig. 5c, to generate a binary image with smooth contours. In the final step, the isolated void regions are filled, see Fig. 5d. In order to generate a low-porosity cracked porous medium, the same approach is implemented; however, rectangles of random size are placed at fixed positions during the first step of the algorithm previously described.

3.2 Calculation of Effective Parameters

After the binary images have been generated, the dispersion coefficient and the dispersion tensor are determined for each image using the Bruggeman relationship

$$D_B^\star(\phi) = \phi^{1.5}, \tag{21}$$

where $D_B^\star$ is the Bruggeman estimate of the dimensionless effective diffusion coefficient, and by solving the closure problem (16), respectively. In the latter case, the void area in each image is triangulated and the closure problem solved using a finite element (FE) method of the first order.

Since the synthetic porous medium is randomly generated, the average characteristics of the medium are isotropic in nature, and it suffices to use the values of the dispersion tensor in one direction only. Figure 6 shows that the xx and yy components of the effective dispersion tensor $\mathbf{D}^\star$ are statistically homogeneous. In Fig. 7, we show the scatter plot of the porosity and the xx-component of the dispersion tensor, i.e., $\left\{\phi_i, D_i^\star\right\}_{i=1}^N$, where ϕ_i and $D_i^\star$ represent the porosity and the xx component of dispersion tensor of the i^{th} image, with N the total number of images and $N = 18,000$. The mean absolute error between the dispersion component obtained using the closure and Bruggeman approaches,

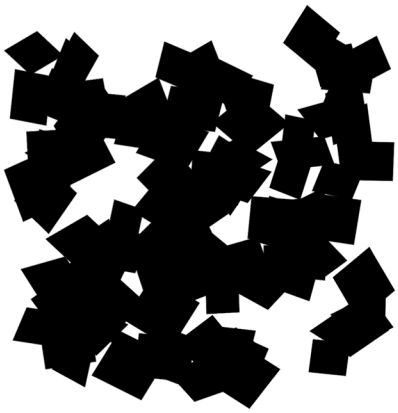

(a) Step 1. Random parallelograms.

(b) Step 2. Gaussian filter with a kernel of a random width.

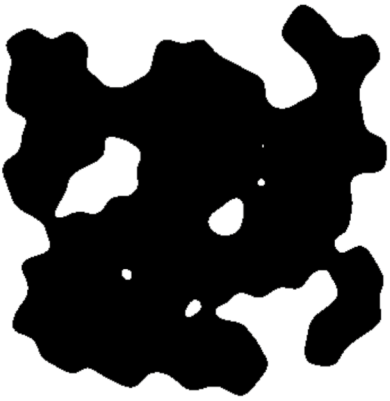

(c) Step 3. Otsu segmentation.

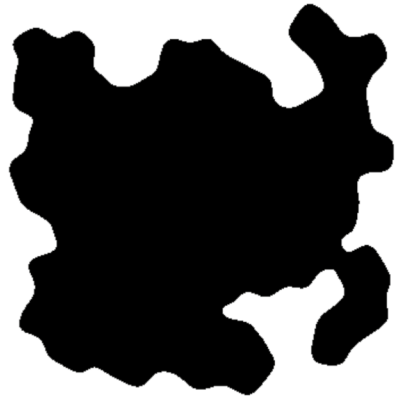

(d) Step 4. Filling isolated regions.

Fig. 5 Steps of the generation of the synthetic granular porous medium

$$\frac{1}{N}\sum_{i=1}^{N}\left|D_B^\star(\phi_i) - D_i^\star\right|, \tag{22}$$

is 0.09. Figure 7 indicates that the Bruggeman approximation has a very low accuracy, especially for dispersion values in the porosity interval of 0.4 to 0.8. Whenever computational costs are a concern, the data $\left\{\phi_i, D_i^\star\right\}_{i=1}^{N}$ can be used to fit a third-order polynomial of the form

$$D_f^\star(\phi) = a\phi^3 + b\phi^2 + c, \tag{23}$$

where $a = 1.6$, $b = -1.1$, $c = 0.6$. The mean absolute error for the fitted model is 0.03, three times lower than the classical Bruggeman approximation.

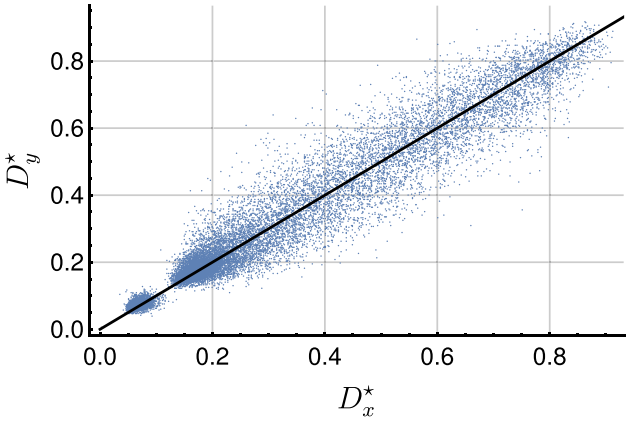

Fig. 6 Scatter plot of the *xx*- and *yy*-components of the effective diffusion tensor. The solid black line represents the 1:1 line. The plot shows that the synthetically generated images are statistically isotropic

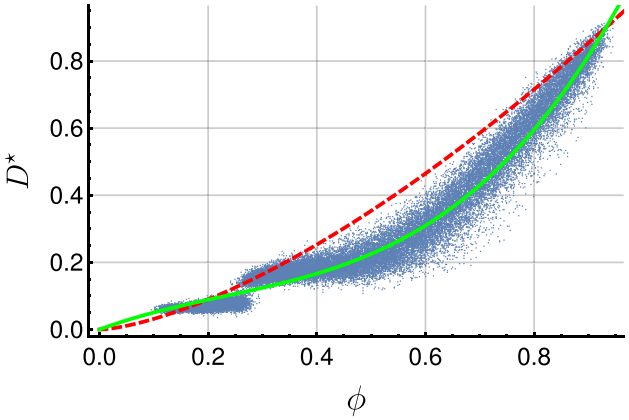

Fig. 7 Comparison of the numerical solution of the "closure problem" with the Bruggeman model (Eq. 21) and the fitting (Eq. 23). Blue dots show the porosity values of the generated images versus the dispersion tensor in *X* direction from the "closure problem." The red dashed line shows the Bruggeman model, while the green line the polynomial fitting

4 Effective Diffusivity Tensor for Realistic Images

In this section, we apply the previous analysis to real images. First, we extend the approach to images that lack periodicity and propose two methods to enforce it: one based on reflection and one on adding a thin buffer zone. We show that the methods provide comparable estimates of the effective diffusion values (Sect. 4.1). Then, we test the robustness of the fitted polynomial against measurements of the effective diffusion coefficient measured on real electrodes, whose values are available in the literature (Sect. 4.2).

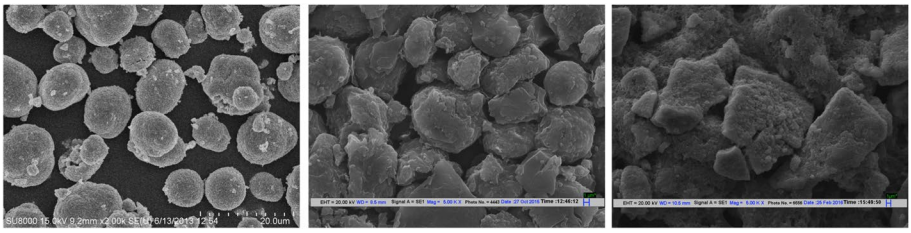

(a) Image 1 (b) Image 2 (c) Image 3

Fig. 8 SEM images of porous electrodes of lithium-ion batteries. The images represent the electrode microstructure of an NMC cathode (**a**), graphite (MCMB) anode (**b**), and LMO cathode (**c**). These images have been reproduced with the permission of the authors Zhang et al. (2015) and Rashid and Gupta (2017)

(a) Image 1 (b) Image 2 (c) Image 3

Fig. 9 Binary segmentation the images (Fig. 8) for a given depth. The black corresponds to the solid phase and white to the void phase. The order is the same as in Fig. 8

4.1 Generalization to Non-periodic Images

The application of the closure variable approach for the estimation of effective properties of porous electrodes is based on a periodicity hypothesis. However, rarely realistic systems satisfy this condition. Figure 8 shows the SEM images for three lithium-ion battery electrodes, i.e., nickel manganese cobalt oxide (NMC) cathode (Zhang et al. 2015), graphite mesocarbon microbeads (MCMBs) anode (Rashid and Gupta 2017), and lithium manganese dioxide (LMO) cathode (Rashid and Gupta 2017). In order to post-process images that lack translational periodicity, we proceed as follows. First, the active material and electrolyte phases of the porous medium are manually identified for a given depth, and binary segmentation is performed using Otsu's approach. The isolated electrolyte regions are manually filled, and a Gaussian filter is applied to the binary images to enhance the mesh. The results of the segmentation are shown in Fig. 9. In order to enforce periodicity, we use two methods. In the first method, the image is subjected to reflection with respect to, first, the Y- and, then, the X-axes as shown in Fig. 10. In the second method, the image is slightly enlarged by adding a thin electrolyte buffer zone. We proceed by solving the closure problem: The results of the distribution of the closure variable for the two methods of periodicity generation are presented in Fig. 11. Despite some differences in the distribution of the closure variable in the unit cell, the effective diffusion components calculated with the two methods agree reasonably well (see Table 1) except for the xx component of the effective diffusion tensor for image 3, although their average values match very well (columns 7 and 8 in Table 1). In Table 1, we also report the calculated effective diffusion coefficients determined both

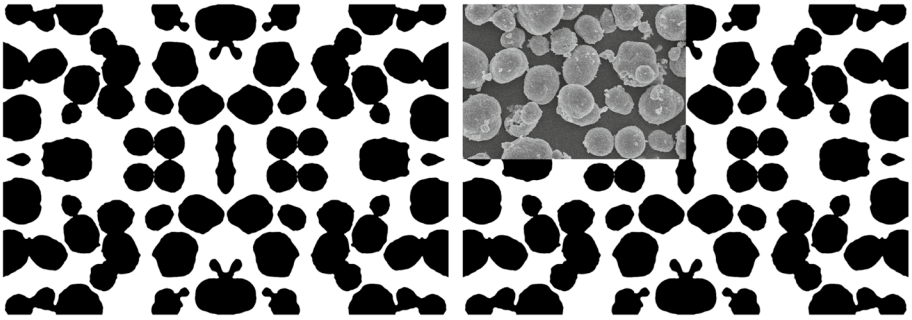

(a) Example of the periodic domain. **(b)** Overlap of the original and periodic images.

Fig. 10 Enforcement of the image periodicity of Fig. 9a. **a** Binary periodic domain composed of reflections of Fig. 9a with respect to *Y*- and *X*-axes, **b** overlap of the periodic and the original images

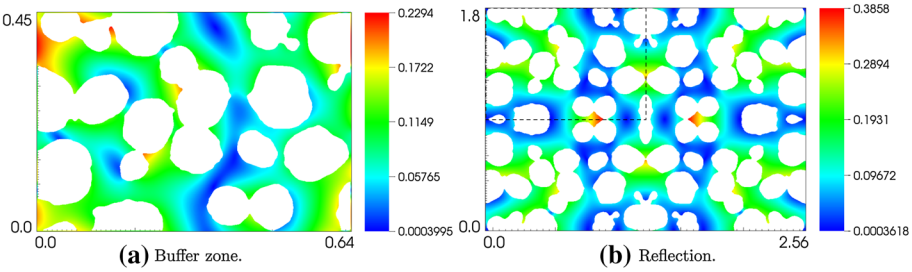

(a) Buffer zone. **(b)** Reflection.

Fig. 11 Distribution of the magnitude of the closure variable χ for two types of the periodicity enforcement for the Image 1 of Fig. 9. **a** The magnitude of the "closure variable" using the buffer zone periodicity, **b** using the reflection with respect to *Y*- and *X*-axes

Table 1 Dispersion tensor calculated by the numerical solution of the "closure problem" for both types of periodicity enforcement for the three images, the porosity values, and the estimations of the dispersion using the Bruggeman approximation (Eq. 21) and the fitted model (Eq. 23)

	ϕ	$\mathcal{D}^\star_{xx}$ reflect	$\mathcal{D}^\star_{yy}$ reflect	$\mathcal{D}^\star_{xx}$ buffer	$\mathcal{D}^\star_{yy}$ buffer	$\mathcal{D}^\star_{\text{average}}$ reflect	$\mathcal{D}^\star_{\text{average}}$ buffer	$D^\star_B(\phi)$	$D^\star_f(\phi)$
Image 1	0.475	0.196	0.224	0.217	0.204	0.210	0.210	0.327	0.208
Image 2	0.432	0.140	0.194	0.137	0.197	0.167	0.167	0.283	0.183
Image 3	0.495	0.131	0.246	0.166	0.254	0.188	0.210	0.348	0.221

from the Bruggeman equation (21) and the data-driven polynomial interpolation (23). Results show that the proposed model estimates the dispersion tensor with better accuracy than the classical Bruggeman relationship.

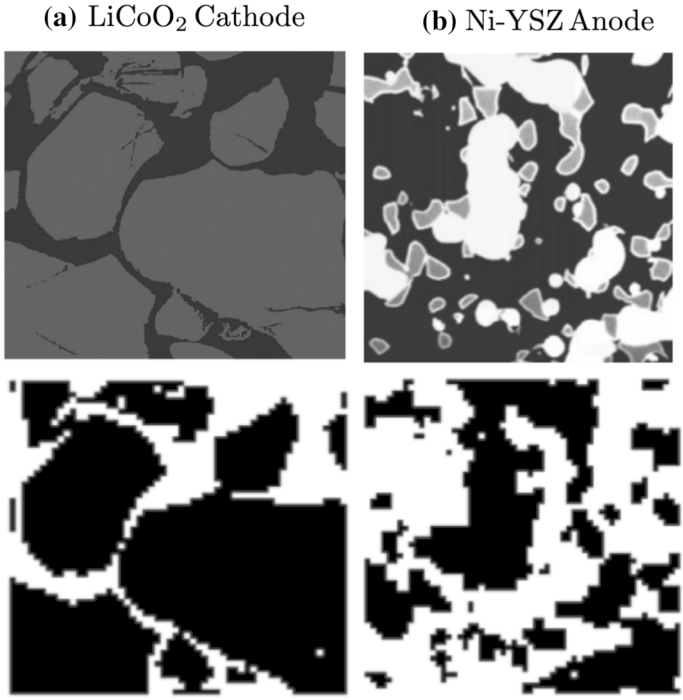

Fig. 12 **a** SEM image of active particles in a $LiCoO_2$ cathode (Hutzenlaub et al. 2013) (top) and segmented image (bottom); **b** SEM image of active particles in a Ni-YSZ anode (Iwai et al. 2010) (top) and segmented image (bottom). The bottom images are used for porosity calculations

4.2 Effective Diffusivity Predictions from SEM Images

Here, we assess the capability of Eq. (23) to predict effective properties of porous electrodes. Figure 12 shows the SEM images of a $LiCoO_2$ cathode and a Ni-YSZ anode, and their corresponding segmented images. Values of the effective diffusivity tensor have been determined by Hutzenlaub et al. (2013) and Iwai et al. (2010), respectively. In Table 2, we report the values of the dimensionless components of the dispersion tensor as measured by Hutzenlaub et al. (2013) and Iwai et al. (2010), which show that the images (and the materials) are only moderately anisotropic. In the same table, we provide a direct prediction of the average value of the effective diffusivity using both the Bruggeman relation and equation (23). Our results show that the proposed equation (23) significantly improves on the classical Bruggeman relationship.

Table 2 Values of the effective diffusivity as determined by Hutzenlaub et al. (2013) and Iwai et al. (2010) and predicted using Eq. (23) and the classical Bruggeman relationship

	ϕ	$\mathcal{D}^\star_{xx}$ measured	$\mathcal{D}^\star_{yy}$ measured	$\mathcal{D}^\star_{\text{average}}$	$\mathcal{D}^\star_f$	$\mathcal{D}^\star_B$
$LiCoO_2$	0.337	0.166	0.103	0.134	0.138	0.196
Ni-YSZ	0.658	0.232	0.239	0.235	0.374	0.534

5 Conclusions

Different analytical, experimental, and numerical approaches have been used to estimate the effective mass and charge transport parameters of electrochemical models for battery dynamic performance. The Bruggeman relationship is still the most popular approach due to its simplicity. However, the classical Bruggeman approach leads to large errors in its estimated values of effective transport coefficients. This is due to the strong approximations underlying its formulation, which range from hypotheses on the shape of the particles to their spatial arrangement, as well as hypotheses on the transport processes dominating at the pore scale. Its formulation is also based on the, often ambiguous, definition of tortuosity, which can be problematic when multiple physical phenomena concurrently occur. Generalizations to non-spherical particles, anisotropic materials, and transport dynamics that deviate from purely diffusive (like in flow batteries where advection plays a role) are often non-trivial and require ad hoc treatment.

Here, we propose a homogenization-based approach to determine effective parameters of upscaled electrochemical models, e.g., effective diffusivity. The method consists in the solution of a vectorial boundary value problem, also known as closure problem, for a closure variable in a representative domain of the electrode, e.g., a unit cell. Effective parameters can be then determined as spatial averages of the closure variable. The advantages of such a framework are disparate: (1) The closure problem is dynamic-specific, i.e., its formulation varies depending on what physical processes occur at the pore scale; (2) it is inherently tensorial, i.e., the effective properties can account for anisotropy and arbitrary topology in the pore-scale structure; and (3) although not necessary, the closure variable can also be used to define tortuosity consistently with the upscaled equation whose coefficients are being determined.

Firstly, the validity of the classical Bruggeman relationship is assessed by generating a total of 18,000 synthetic images and determining the dispersion tensor components for each image by solving the closure problem. The data are then used to propose a more generalized polynomial relationship to improve the fitting analysis of the dispersion tensor vs. porosity plot, when computational burden is of concern. The closure variable approach is then generalized to images that lack translational periodicity. The dispersion tensor is evaluated by generating 2-D reconstructions of realistic electrode microstructural images, obtained from the 3-D SEM imaging technique. Two different approaches, the *reflection* method and the *buffer* method, are presented to induce periodicity in the 2-D reconstructed images to enable resolution of the closure problem. Comparison between the dispersion values obtained with the classical Bruggeman approach and the proposed relationship reveals that the former significantly overpredicts the tensor component values (by at least 38%) for the three different electrode microstructures considered in this paper. The proposed polynomial relationship performs better in these scenarios and reveals better correlation with the *yy* component values of the dispersion tensor than the *xx* component values. Finally, the proposed polynomial relationship is used to make forward predictions of effective properties of realistic porous electrodes. The predictions match well with independent estimates of effective parameters for two electrode types: a $LiCoO_2$ cathode and a Ni-YSZ anode.

This analysis suggests that data-driven approaches based on rigorous homogenization methods can be successfully employed to significantly improve the prediction of effective parameters while not sacrificing computational resources.

Acknowledgements SK, HA and SO were supported in part by the National Science Foundation under the grant CAREER No. 1839050. Any opinions, findings, and conclusions or recommendations expressed in this material are those of the authors and do not necessarily reflect those of the National Science Foundation. Also, the authors are thankful to Zhang et al. (2015) and Rashid and Gupta (2017) for providing high-resolution SEM images. IB was fully supported by the Department of Energy under the Early Career award DE-SC0014227.

Appendix

The Wolfram Mathematica script to generate black/white images of the random granular synthetic porous medium is listed below,

```
ImageResize[
 ColorNegate[
  FillingTransform[
   ColorNegate[
    Binarize[
     GaussianFilter[
      Graphics[
       Table[Scale[
         Rotate[Rectangle[{RandomReal[{0, 12}], RandomReal[{0, 12}]}],
          RandomReal[{0, 2 Pi}]], {RandomReal[{1, 2}],
          RandomReal[{1, 2}]}], {i, 1, RandomInteger[{1, 150}]}]],
      RandomReal[{0, 20}]]]]], {360, 360}]
```

where the image size is 360×360 pixels and the black corresponds to the solid phase. We also list the script to generate images of the random low-porosity cracked synthetic porous medium

```
ImageResize[
 ImagePad[ColorNegate[
   FillingTransform[
    ColorNegate[
     Binarize[
      GaussianFilter[
       Graphics[
        Table[Rectangle[{i, j}, {i + RandomReal[{0.7, 1.2}],
           j + RandomReal[{0.7, 1.2}]}], {i, 1, 10}, {j, 1, 10}]],
       RandomReal[{1, 10}]]]]], -4], {360, 360}]
```

References

Abraham, K.M.: Directions in secondary lithium battery research and development. Electrochim. Acta **38**, 1233 (1993)

Adler, P.: Porous Media: Geometry and Transports. Butterworth-Heinemann, Oxford (1992)

Allen, R., Sun, S.: Computing and comparing effective properties for flow and transport in computer-generated porous media. Geofluids (2017). https://doi.org/10.1155/2017/4517259

Archie, G.: The electrical resistivity log as an aid in determining some reservoir characteristics. Trans. Am. Inst. Mech. Eng. **146**, 54–67 (1942)

Arunachalam, H., Onori, S.: Full homogenized macroscale model and pseudo-2-dimensional model for lithium-ion battery dynamics: comparative analysis, experimental verification and sensitivity analysis. J. Electrochem. Soc. **166**(8), A1380–A1392 (2019)
Arunachalam, H., Korneev, S., Battiato, I., Onori, S.: Multiscale modeling approach to determine effective lithium-ion transport properties. In: Proceedings of the 2017 American Control Conference, pp. 92–97. IEEE (2017)
Arunachalam, H., Onori, S., Battiato, I.: On veracity of macroscopic lithium-ion battery models. J. Electrochem. Soc. **162**(10), A1940–A1951 (2015)
Battiato, I., Tartakovsky, D.M.: Applicability regimes for macroscopic models of reactive transport in porous media. J. Contam. Hydrol. **120–121**, 18–26 (2011)
Battiato, I., Ferrero V, P.T., O' Malley, D., Miller, C.T., Takhar, P.S., Valdés-Parada, F.J., Wood, B.D.: Theory and applications of macroscale models in porous media. Transp. Porous Media (2019). https://doi.org/10.1007/s11242-019-01282-2
Battiato, I., Tartakovsky, D.M., Tartakovsky, A.M., Scheibe, T.: On breakdown of macroscopic models of mixing-controlled heterogeneous reactions in porous media. Adv. Water Resour. **32**(11), 1664–1673 (2009)
Bear, J.: Hydrodynamic dispersion. In: De Wiest, R. (ed.) Flow Through Porous Media, pp. 109–199. Wiley, New York (1969)
Bear, J.: Dynamics of Fluids in Porous Media. Elsevier, New York (1972)
Boso, F., Battiato, I.: Homogenizability conditions for multicomponent reactive transport. Adv. Water Resour. **62**, 254–265 (2013)
Bucci, G., Swamy, T., Chiang, Y.-M., Carter, W.C.: Random walk analysis of the effect of mechanical degradation on all-solid-state battery power. J. Electrochem. Soc. **164**, 12 (2017)
Carman, P.C.: Fluid flow through granular beds. Trans. Inst. Chem. Eng. **50**, 150–166 (1937)
Choi, J.W., Aurbach, D.: Promise and reality of post-lithium-ion batteries with high energy densities. Nat. Rev. Mater. **1**, 16013 (2016)
Chung, D.-W., Enber, M., Ely, D.R., Wood, V., Garcia, R.E.: Validity of the Bruggeman relation for porous electrodes. Model. Simul. Mater. Sci. Eng. **21**(7), 074009 (2013)
Chung, D.-W., Shearing, P.R., Brandon, N.P., Harris, S.J., Garcia, R.E.: Particle size polydispersity in Li-ion batteries. J. Electrochem. Soc. **161**(3), A422–A430 (2014)
Clennel, M.B.: Tortuosity: A Guide Through the Maze (Special Publication), vol. 122. Geological Society (1997)
Cooper, S.J., Kishimoto, M., Tariq, F., Bradley, R.S., Marquis, A.J., Brandon, N.P., Kilner, J., Shearing, P.R.: Microstructural analysis of an LSCF cathode using in-situ tomography and simulation. ECS Trans. **57**(1), 2671–2678 (2013)
Cooper, S., Eastwood, D., Gelb, J., Damblanc, G., Brett, D., Bradley, R., Withers, P., Lee, P., Marquis, A., Bran don, N., Shearing, P.: Image based modelling of microstructural heterogeneity in $LiFePO_4$ electrodes for Li-ion batteries. J. Power Sources **247**, 1033–1039 (2014)
Darcy, H.: Les fontaines publiques de la ville de dijon. Technical report, Dalmont, Paris (1856)
Djian, D., Alloin, D., Martinet, S., Lignier, H., Sanchez, J.Y.: Lithium-ion batteries with high charge rate capacity: influence of porous separator. J. Power Sources **172**(416), 416–421 (2007)
Doyle, M., Newman, J.: The use of mathematical modeling in the design of lithium/polymer battery systems. Electrochim. Acta **40**(13–14), 2191–2196 (1995)
Doyle, M., Fuller, T.F., Newman, J.: Modeling of galvanostatic charge and discharge of the lithium/polymer/insertion cell. J. Electrochem. Soc. **140**(6), 1526–1533 (1993)
DuBeshter, T., Sinha, P.K., Sakars, A., Fly, G.W., Jorne, J.: Measurement of tortuosity and porosity of porous battery electrodes. J. Electrochem. Soc. **161**(4), A599–A605 (2014)
Dullien, F.: Porous Media Fluid Transport and Pore Structure. Academic Press, New York (1992)
Ebner, M., Wood, V.: Tool for tortuosity estimation in lithium ion battery porous electrodes. J. Electrochem. Soc. **162**(2), A3064–A3070 (2015)
Ebner, M., Chung, D.W., Garcia, R.E., Wood, V.: Tortuosity anisotropy in lithium-ion battery electrodes. Adv. Energy Mater. **4**(5), 1301278 (2014)
Edwards, D., Shapiro, M., Brenner, H.: Dispersion and reactions in two-dimensional model porous media. Phys. Fluids **5**, 837–848 (1993)
Fotouhi, A., Auger, D.J., Propp, K., Longo, S., Wild, M.: A review on electric vehicle battery modelling: from lithium-ion toward lithium–sulphur. Renew. Sustain. Energy Rev. **56**, 1008–1021 (2016)
Garcia, R.E., Chiang, Y.-M.: Spatially resolved modeling of microstructurally complex battery architectures. J. Electrochem. Soc. **154**(9), A856–A864 (2007)
Garcia, R.E., Chiang, Y.-M., Carter, W.C., Limthongkul, P., Bishop, C.M.: Microstructural modeling and design of rechargeable lithium-ion batteries. J. Electrochem. Soc. **152**(1), A255–A263 (2005)

García-García, R., García, R.E.: Microstructural effects on the average properties in porous battery electrodes. J. Power Soc. **309**, 11–19 (2016)
Ghanbarian, B., Hunt, A.G., Ewing, R.P., Sashimi, M.: Tortuosity in porous media: a critical review. Soil Sci. Soc. Am. J. **77**, 1461–1477 (2012)
Grazioli, D., Magri, M., Salvadori, A.: Computational modeling of li-ion batteries. Comput. Mech. **58**(6), 889–909 (2016)
Greenkorn, R.: Flow Phenomena in Porous Media. Marcel Dekker, New York (1983)
Grützke, M., Kraft, V., Hoffmann, B., Klamor, S., Diekmann, J., Kwade, A., Winter, M., Nowak, S.: Aging investigations of a lithium-ion battery electrolyte from a field-tested hybrid electric vehicle. J. Power Sources **273**, 83–88 (2015)
Hutzenlaub, T., Asthana, A., Becker, J., Wheeler, D., Zengerle, R., Thiele, S.: FIB/SEM-based calculation of tortuosity in a porous $LiCoO_2$ cathode for a li-ion battery. Electrochem. Commun. **27**, 77–80 (2013)
Iwai, H., Shikazono, N., Matsui, T., Teshima, H., Kishimoto, M., Kishida, R., Hayashi, D., Matsuzaki, K., Kanno, D., Saito, M., Muroyama, H., Eguchi, K., Kasagi, N., Yoshida, H.: Quantification of SOFC anode microstructure based on dual beam FIB-SEM technique. J. Power Sources **195**(4), 955–961 (2010)
Jiang, F., Peng, P.: Elucidating the performance limitations of lithium-ion batteries due to species and charge transport through five characteristic parameters. Sci. Rep. **6**, 32639 (2016)
Kehrwald, D., Shearing, P.R., Brandon, N.P., Sinha, P.K., Harris, S.J.: Local tortuosity inhomogeneities in a lithium battery composite electrode. J. Electrochem. Soc. **158**(12), A1393–A1399 (2011)
Korneev, S., Battiato, I.: Sequential homogenization of reactive transport in polydisperse porous media. SIAM Multiscale Model. Sim. **14**(4), 1301–1318 (2016)
Kozeny, J.: Uber kapillare leitung des wassers im boden. Sitzungberichte der Akadämie der Wissenschaftung in Wein Abteilung IIa **136**, 271–301 (1927)
Landesfeind, J., Hattendorff, J., Ehrl, A., Wall, W.A., Gasteiger, H.A.: Tortuosity determination of battery electrodes and separators by impedance spectroscopy. J. Electrochem. Soc. **163**(7), A1373–A1387 (2016)
Less, G.B., Seo, J.H., Han, S., Sastry, A.M., Zausch, J., Latz, A., Schmidt, S., Wieser, C., Kehrwald, D., Fell, S.: Micro-scale modeling of Li-ion batteries: parameterization and validation. J. Electrochem. Soc. **159**(6), A697–A704 (2012)
Malifarge, S., Delobel, B., Delacourt, C.: Determination of tortuosity using impedance spectra analysis of symmetric cell. J. Electrochem. Soc. **164**(11), E3329–E3334 (2017)
Otsu, N.: A Threshold Selection Method from Gray-Level Histograms. IEEE Transactions on Systems, Man, and Cybernetics **9**, 62–66 (1979)
Penman, H.: Gas and vapor movement in soil. J. Agric. Sci. **30**, 438–462 (1940)
Petersen, E.: Diffusion in a pore of varying cross section. AIChE J. **4**, 343–345 (1958)
Rashid, M., Gupta, A.: Experimental assessment and model development of cycling behavior in Li-ion coin cells. Electrochim. Acta **231**, 171–184 (2017)
Sbarufatti, C., Corbetta, M., Giglio, M., Cadini, F.: Adaptive prognosis of lithium-ion batteries based on the combination of particle filters and radial basis function neural networks. J. Power Soc. **344**, 128–140 (2017)
Sharratt, P., Mann, R.: Some observations on the variation of tortuosity with thiele modulus and pore size distribution. Chem. Eng. Sci. **42**, 1565–1575 (1987)
Shearing, P.R., Howard, L.E., Jørgensen, P.S., Brandon, N.P., Harris, S.J.: Characterization of the 3-dimensional microstructure of a graphite negative electrode from a Li-ion battery. Electrochem. Commun. **12**(3), 374–377 (2010)
Stephenson, D., Hartman, E., Harb, J., Wheeler, D.: Modeling of particle-particle interactions in porous cathodes for lithium-ion batteries. J. Electrochem. Soc. **154**, A1146–A1155 (2007)
Stiaszny, B., Ziegler, J.C., Krauß, E.E., Schmidt, J.P., Ivers-Tiffée, E.: Electrochemical characterization and post-mortem analysis of aged $LiMn_2O_4$-$Li(Ni_{0.5}Mn_{0.3}Co_{0.2})O_2$/graphite lithium ion batteries. Part I: Cycle aging. J. Power Sources **251**, 439–450 (2014a)
Stiaszny, B., Ziegler, J.C., Krauß, E.E., Zhang, M., Schmidt, J.P., Ivers-Tiffée, E.: Electrochemical characterization and post-mortem analysis of aged $LiMn_2O_4$-nmc/graphite lithium ion batteries part II: calendar aging. J. Power Sources **258**, 61–75 (2014b)
Sun, Z., Tang, X., Cheng, G.: Numerical simulation for tortuosity of porous media. Microporous Mesoporous Mater. **173**, 37–42 (2013)
Terborg, L., Weber, S., Blaske, F., Passerini, S., Winter, M., Karst, U., Nowak, S.: Investigation of thermal aging and hydrolysis mechanisms in commercial lithium ion battery electrolyte. J. Power Sources **242**, 832–837 (2013)

Thorat, I.V., Stephenson, D.E., Zacharias, N.A., Zaghib, K., Harb, J.N., Wheeler, D.R.: Quantifying tortuosity in porous Li-ion battery materials. J. Power Sources **188**(2), 592–600 (2009)

Tjaden, B., Cooper, S.J., Brett, D.J.L., Kramer, D., Shearing, P.R.: On the origin and application of the bruggeman correlation for analysing transport phenomena in electrochemical systems. Curr. Opin. Chem. Eng. **12**, 44–51 (2016)

Valdés-Parada, F.J., Porter, M.L., Wood, B.D.: The role of tortuosity in upscaling. Transp. Porous Med. **88**, 1–30 (2011)

Vijayaraghavan, B., Ely, D.R., Chiang, Y.-M., Garcia, R.G., Garcia, R.E.: An analytical method to determine tortuosity in rechargeable battery electrodes. J. Electrochem. Soc. **159**(5), A548–A552 (2012)

Wilson, J.R., Cronin, J.S., Barnett, S.A., Harris, S.J.: Measurement of three-dimensional microstructure in a $LiCoO_2$ positive electrode. J. Power Sources **196**, 3443–3447 (2011)

Yu, C., Ganapathy, S., de Klerk, N.J.J., Roslon, I., van Eck, E.R.H., Kentgens, A.P.M., Wagemaker, M.: Unravelling Li-ion transport from picoseconds to seconds: bulk versus interfaces in an argyrodite Li_6PS_5Cl-Li_2S all-solid-state Li-ion battery. J. Am. Chem. Soc. **138**, 11192–11201 (2016)

Zhang, X., Tartakovsky, D.M.: Effective ion diffusion in charged nanoporous materials. J. Electrochem. Soc. **164**(4), E53–E61 (2017a)

Zhang, X., Tartakovsky, D.M.: Optimal design of nanoporous materials for electrochemical devices. Appl. Phys. Lett. **110**(14), 143103 (2017b)

Zhang, Y., Wang, Z.-B., Lei, J., Li, F.-F., Wu, J., Zhang, X.-G., Yu, F.-D., Ke, K.: Investigation on performance of $Li(Ni_{0.5}\,Co_{0.2}\,Mn_{0.3})_{1-x}\,Ti_x\,O_2$ cathode materials for lithium-ion battery. Ceram. Int. **41**(7), 9069–9077 (2015)

Zhang, X., Urita, K., Moriguchi, I., Tartakovsky, D.M.: Design of nanoporous materials with optimal sorption capacity. J. Appl. Phys. **117**(24), 244304 (2017)

Zheng, L., Zhang, L., Zhu, J., Wang, G., Jiang, J.: Co-estimation of state-of-charge, capacity and resistance for lithium-ion batteries based on a high-fidelity electrochemical model. Appl. Energy **180**, 424–434 (2016)